




Article

Design and Experimental Evaluation of an In-Wheel Flux-Switching Machine for Light Vehicle Application

Gabriel A. Mendonça ¹, Diogo P. V. Galo ², Luís Carlos M. Sales ³, Braz J. Cardoso Filho ⁴
and Thales A. C. Maia ^{4,*}

- ¹ Aperam South America-Praça 1º, de Maio, 9-Centro, Timóteo 30180-018, MG, Brazil
² Graduate Program in Electrical Engineering, Universidade Federal de Minas Gerais, Av. Antônio Carlos 6627, Belo Horizonte 31270-901, MG, Brazil
³ Stellantis Brasil, Av. Contorno, 3455, Bairro Paulo Camilo, Betim 32530-900, MG, Brazil
⁴ Electrical Engineering Department, Universidade Federal de Minas Gerais, Av. Antônio Carlos 6627, Belo Horizonte 31270-901, MG, Brazil
* Correspondence: thalesmaia@cpdee.ufmg.br

Abstract: Restrictive regulations regarding emissions and fossil fuel consumption lead to the electric vehicle being an alternative to replace conventional internal combustion engine vehicles. The pure electric powertrain technology and the charging infrastructure are still immature in some markets, where increasing the overall vehicle efficiency by energy harvesting means can be a more viable solution. This paper presents the design and experimental validation of an in-wheel flux-switching machine for regenerative braking in a light passenger vehicle. Later, the energy can be used for fuel handling and reforming, performance enhancement, increasing efficiency, and reducing emissions. Feasibility and technological challenges are also discussed. The Maxwell–Fourier method and a novel steady-state equivalent circuit presented in this paper are used for geometry sensitivity analysis and optimization routine.

Keywords: flux-switching machine; efficiency; regenerative braking; energy harvesting



Citation: Mendonça, G.A.; Galo, D.P.V.; Sales, L.C.M.; Cardoso Filho, B.J.; Maia, T.A.C. Design and Experimental Evaluation of an In-Wheel Flux-Switching Machine for Light Vehicle Application. *Machines* **2022**, *10*, 671. <https://doi.org/10.3390/machines10080671>

Academic Editors: Lorand Szabo and Feng Chai

Received: 11 July 2022

Accepted: 1 August 2022

Published: 10 August 2022

Publisher's Note: MDPI stays neutral with regard to jurisdictional claims in published maps and institutional affiliations.



Copyright: © 2022 by the authors. Licensee MDPI, Basel, Switzerland. This article is an open access article distributed under the terms and conditions of the Creative Commons Attribution (CC BY) license (<https://creativecommons.org/licenses/by/4.0/>).

1. Introduction

The road transportation sector is responsible for approximately half of world's oil demand, most particulate matter emissions and air pollutants. Vehicle emissions are more critical in urban areas due to health concerns and micro/macro climate changes [1]. Over recent decades, regulatory initiatives, such as the Euro or the US Tier, were introduced and are being constantly updated. The establishment of emissions standards is related to the reduction in transport-related emissions. However, the implementation of more restrictive standards within the next years depends on each market's political, economic and geographic particularities, which demands local technological development [2].

The automotive industry struggles to keep up with upcoming emission standards, which demands increasing the vehicle's efficiency by partially or fully electrifying the powertrain. However, there are several problems related to powertrain electrification yet to be resolved, such as cost, range, technological maturity, safety, charging time, and battery power density. The aforementioned challenges regarding electrification still prevents the widespread adoption of electric vehicles worldwide [3,4].

Automotive energy harvesting systems are usually employed to increase overall vehicle efficiency. One example is thermal recovery, in which an amount of energy is recovered from exhaust gasses and engine coolant. Moreover, keeping the system as simple as possible, reducing weight and minimizing the cost is more important than maximizing power output [5,6]. Heat recovery systems can also be used, combining Rankine cycle systems with electrical generators to create a turbo-generator [6,7]. Energy dissipated on the vehicle suspension is another possibility for energy harvesting. This

system recovers waste heat energy from car bumper, while improving vehicle driveability and handling characteristics [8,9]. Electromagnetic-based systems are preferred due to their high efficiency, design simplicity, and controllability [10,11]. Thus, the hybrid electric vehicle (HEV) is a suitable candidate to meet the upcoming emission standards during the electric vehicle technological maturation stage.

HEVs still rely on the use of an internal combustion engines (ICE) as the main source of propulsion, which leverages the well established fueling infrastructure. The use biofuels have advantages for being considered carbon neutral, in addition of benefiting from the existing traditional fueling supply chain [3,12]. As the powertrains obtain higher levels of electrification, ICE efficiency can be increased mainly due to the electric machine contribution [4]. Among different hybrid technologies, it is possible to characterize different levels of hybridization. Vehicles can be classified according to ratio between the electric powertrain power to the total vehicle power [13].

The vehicle with a hybridization level of less than 5%, is known as micro-hybrid. This type of vehicle uses the ICE as the main source of propulsion. It improves performance by using the start-stop functionality, in which the ICE shuts down at idling conditions. Another possible application is the regenerative braking, used to recharge the batteries during vehicle deceleration [14]. Under these conditions the fuel efficiency can reach up to 10%.

The amount of energy stored in vehicle inertia is approximately 6% of the total energy consumed by the vehicle. This energy can be harvested with the aid of regenerative braking instead of being wasted as heat in friction brakes. In micro and mild hybrid electric vehicles, regenerative braking is usually accomplished by using a BSG (Belt-driven Starter Generator) [13]. Considering lower levels of hybridization, the BSG is a cost effective way to reduce CO₂ emissions and lowering the total cost of ownership (TCO) [15]. On the other hand, it demands redesigning most of the electrical system of the vehicle and the front-end accessory drive system. Alternatives based on in-wheel motors are less invasive and demand fewer changes on an existing ICE vehicle platform [16–18]. In-wheel electric motors enable four wheel drive, enhanced vehicle stability and improved acceleration and efficiency [19,20].

This paper presents the design, construction, and validation of an in-wheel flux-switching machine to be used in a regenerative braking system of a light-duty ICE passenger vehicle [21]. The research is based on an existing ICE vehicle platform to reduce costs and increase project feasibility. The main objective is to contribute with a critical analysis regarding the technological challenges faced during the design routine of a flux-switching machine with the aid of a novel equivalent steady-state circuit and the Maxwell–Fourier method during a regenerative braking operation. The topology is chosen due to its robust structure and the possibility of using its operating characteristics to realize a low cost drive system. In this sense, the electromagnetic modeling, geometry sensibility analysis, design optimization constraints, and construction and validation test of the electrical machine are discussed.

2. State of Art

Regenerative braking is a common feature in hybrid electric vehicles. In micro and mild hybrid vehicles, this solution is obtained by replacing the alternator and starter motor by a single electric machine. This device provides an effective and simple solution using the conventional ICE vehicle platform [22]. The system is usually designed to provide start–stop operation in addition to the regenerative braking functionality. The design of the BSG system is challenging due to its rigorous requirements, such as high starting torque for engine cranking, wide speed range operation, harsh environment, constrained dimensions, and high temperatures [23–25].

Despite the centralized electric drive system being regarded as a natural solution for hybrid and full electric vehicles, there are benefits of exploring alternative configurations. Full electric vehicles can be designed with in-wheel motors to improve transmission efficiency

and reduces vehicle weight by eliminating differentials and the drive shaft. Furthermore, it gives more flexibility for vehicle chassis design, allowing more space for components as energy storage system [26]. The distributed drive topology with good bandwidth response provides better vehicle stability, safety, and more effective braking [20,27].

In lower hybridization levels, electric vehicles can be designed with in-wheel motors on the rear axle, with the front axle being propelled by the ICE. This architecture is known as the Through-the-Road (TtR) parallel hybrid. However, unlike a conventional parallel hybrid structure, the TtR configuration can be adapted in any conventional ICE vehicle. The implementation is cheaper and more straightforward since there is no mechanical coupling between the engine and the electrical motor, which makes the complex torque coupling device unnecessary [19,28].

The discussed advantages give in-wheel motors a growing interest within electric vehicles technological development. However, this solution introduces additional challenges that must be addressed. To begin with, the electric machine must be robust enough to support a harsh environment. This includes intense vibrations, repeated shock loads, and impacts from debris. In addition, mechanical friction brakes and on-body ICE powertrain increase the wheel temperature significantly. Furthermore, the increased unsprung mass within the wheels can affect the vehicle driving characteristics (driveability and comfort). Finally, the in-wheel machine must be light and compact enough to be installed inside the wheel hub.

Considering the listed requirements, the choice of the appropriate electric machine topology is of great importance. The design assumptions had led to different motor concepts, but most commercially available solutions focus on permanent magnet (PM) brushless machines. The use of high energy magnet and flexible design for both rotor and stator structures offers a high power and torque density solution with the possibility of tailoring the design according to the application requirements. Examples of current improvements include the study of different PM arrangements to enhance output torque [29–31] or different stator winding arrangements to extend speed range operation [32,33].

On the other hand, rare earth permanent magnets represent a costly component of the electrical machine, responsible for approximately 20% to 30% of its cost [34]. Additionally, the design must consider critical operational aspects, such as demagnetization risk and mechanical harness. These had encouraged design approaches able to reduce or eliminate the use of rare earth magnets [35,36]. The trend towards electrical machines without rare earth magnets are the topologies whose working principle is based on variable reluctance torque capabilities.

Reluctance machines are of simple construction and their rotor is composed of, exclusively, passive elements. This design offers desirable features, such as a robust structure and good thermal performance. The switching reluctance machine (SRM) is a popular topology and has been investigated over the past few years. It offers excellent characteristics for electric vehicle application, such as long constant power range, fault tolerance capability and rugged rotor structure, which allows high-temperature operation [26,35]. This topology has been proposed in the literature as suitable for in-wheel motors. The main disadvantages of SRM are: high torque ripple, noise, vibration, and the need of non-conventional inverter topology with a high current rating for the power semi-conductor modules.

In [37], the authors evaluated the motor performance sensibility to different core designs, focused on reducing the weight of the machine. In [38], a segmented-rotor SRM with concentrated winding is proposed as a high specific torque and efficiency solution. The designed topology presented a torque per active weight of 73% of a brushless DC motor with the same outer diameter. In [39], a double stator axial-flux SRM is designed for a light weight in-wheel application, in which experimental results presented a torque comparable with a base internal PMSM with the same size. In [40], a novel radial field C-core SRM is evaluated, showing good features, such as low excitation current and an easily removable rotor.

Another variable reluctance topology that is emerging is known as flux-switching machine (FSM). It offers great flexibility for both the stator and rotor structures. It can be designed with a hybrid excitation, associating PM with field coils placed in the stator. The hybrid excitation FSM offers good power density and efficiency with flux weakening capability [41]. In [42], different hybrid excitation FSM topologies are evaluated for aircraft applications requiring features, such as reliability, high power and torque densities, and fault tolerance ability. Another type of FSM which adopts only PM excitation has the advantages of being less prone to demagnetization while offering a better PM thermal management. In [43], the performance of a PM-FSM is compared with a surface-mounted PMSM, both designed as an in-wheel motor for a hybrid truck. The evaluated FSM topologies showed higher induced voltage and larger electrical loading capability. In [44], the designed FSM topologies using Dy-free PM or field winding showed great potential for traction application. Eliminating the PM, field-excited FSM offers controllable flux with lower cost. This work focused on robustness, simplicity, and cost effectiveness for the development of a regenerative braking solution. Therefore, other topologies which can be considered as a viable alternative were not considered. For instance, induction machines require complex power electronics and control. Other similar flux-modulation machines, such as the claw pole machine [45] or the synchronous homopolar machine [46], were not suitable due to limited space. In [47], a three-phase field-excited FSM design is demonstrated to be a good candidate for hybrid EV, with the optimized result achieving a power density of 4.8 kW/kg.

FSM also presents a robust structure and, with the adoption of a field winding, can be operated using a simple control circuit, eliminating the need of an active rectifier. The generated voltage is close to a sine waveform and, for a series connected field winding, the field inductance is constant.

Therefore, the machine topology chosen to implement the regenerative braking system in a hybrid electric vehicle is the in-wheel FSM. The FSM proposed for this work is a type of AC machine with salient pole rotor (5 teeth) and stator with field and armature windings distributed over 24 slots, as illustrated in Figure 1. The design variables of the presented topology are given on Table 1.

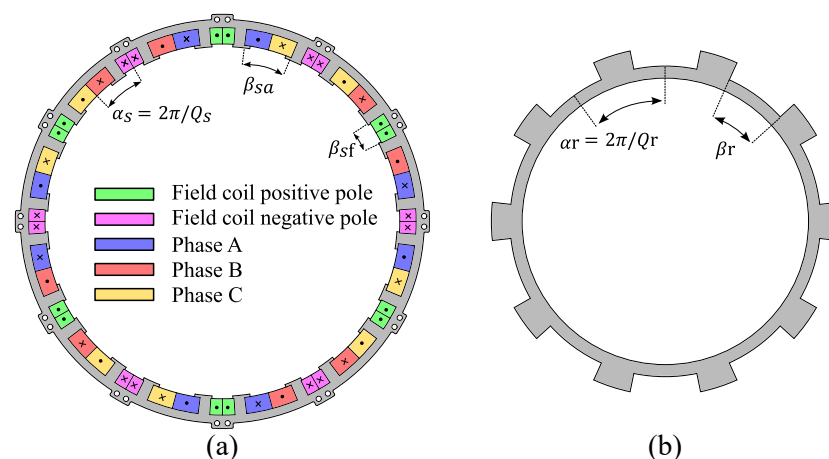


Figure 1. Cross-section of the base geometry used on this paper: (a) stator with field and armature windings, and (b) salient pole rotor.

The modeling method plays an important role in the analysis and design of electric machines. Numerical methods, such as the finite-element method, are consolidated techniques which are widely used owing to its capacity of modeling complex structures and non-ideal materials properties. On the other hand, these methods are time-consuming and require large computational effort. Analytical and semi-analytical methods provide fast and accurate results on magnetic field calculations. Two types of analytical methods are commonly used for design purposes: magnetic equivalent circuit (MEC) and Maxwell–Fourier

method [18]. Regarding reluctance machines, Maxwell–Fourier offers a more flexible solution and is used for geometries which parameters vary in a large scale [48,49]. Thus, this method is used for magnetic field distribution evaluation.

Table 1. FSM design variables.

Parameter	Symbol
Air gap radius	r_{ag}
Armature slot angular aperture	β_{sa}
Armature slot outer radius	r_{sa}
Field slot angular aperture	β_{sf}
Field slot outer radius	r_{sf}
Rotor teeth angular aperture	β_r
Rotor slot inner radius	r_{ri}
Field winding number of coils	N_f
Armature winding number of coils	N_s

3. Methodology

In order to meet the machine requirements of power and performance for the existing light-duty ICE passenger vehicle, authors proposed a methodology based on steady state evaluation and optimization routines. The proposed methodology is presented in Figure 2 and is described as follows. Starting with a draft design, the electrical machine parameters are calculated using a semi-analytical method. In early design stages this approach gives reasonably accurate results with less computational effort when compared with numerical solutions [50]. The generated power is calculated with the aid of a newly developed equivalent circuit. The steady state analysis is obtained considering the effects of variable inductance from the machine double salient structure. The calculated performance gives an indication if the proposed design is consistent, otherwise the dimensions and magnetizing current are modified. The new design goes through a new analysis cycle, which is carried out until the desired characteristics are obtained.

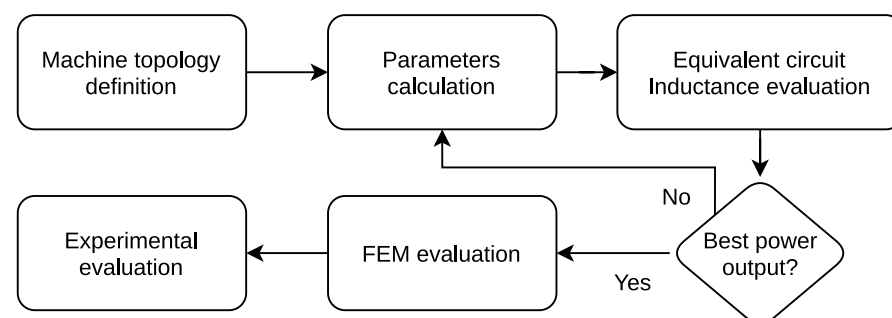


Figure 2. Research work flow methodology.

3.1. Design Specifications and Restrictions

Since the research goal is to promote energy harvesting in an existing light ICE vehicle with the aid of an in-wheel electric machine, the design preserves the original powertrain. Appropriate placement occurs in the rear axle wheels using the available space between the drum brake and inner wheel radius. The geometric constraints are usually restrictive for the number of poles.

In order to define machine rated power constraint two approaches are considered: the amount of power that can be recovered during braking and the average power needed for the auxiliary loads.

Mechanical friction braking systems must coexist with electrical regenerative braking in hybrid and full electric vehicles. During deceleration, 65% of the braking power occurs in the front axle, while only 35% is used in the rear axle [51]. These values are lower for drum-based brake systems. In addition, for a 1000 kg ICE passenger car in the FTP 75 urban drive cycle, the maximum braking power per wheel is around 2 kW and the average power is roughly 750 W. Considering a parallel braking strategy, it is reasonable to account for half of the power, 375 W for the regenerative braking per wheel. The evaluation of the system during the complete drive-cycle is not considered, since it will depend on a specific vehicle platform and its dynamic loads, as well as the storage system capacity and state-of-charge.

The research focuses on the ICE efficiency, so it is reasonable to consider loads that are used to increase ICE efficiency, such as the E-Flex system. The system uses an electric heater for the ethanol with a power demand of 288 W. Therefore, a total of 300 W (150 W per wheel) of electrical regenerative power with air cooling and a maximum of 10 A/mm² for current density is considered.

The vehicle's electric system was not modified and the machine is designed to charge the existing 12 V battery. Thus, the electromagnetic project was conducted focusing on this voltage level. The field winding number of turns is chosen considering a rated current below 1 A. This value is compatible with lower wire gauges and manual manufacturing processes. As for the stator winding turns, an initial value is set considering the desired no load induced voltage, but this value is further adjusted with the optimization routine. The available axial length must consider mechanical stator support, miscellaneous, such as bolts, nuts, washers and others, room for electrical connection, and, finally, end-turn coil size. All of those were evaluated with the aid of a 3D CAD software. However, end-turns' length depends on wire thickness, number of coils, and how they are tied together. It is possible to increase or decrease the number of turns keeping the field intensity constant of the field winding. To ensure a minimum end-turn coil length, including a lower curvature radius, many manufacturing trials were performed using a 3D-printed stator structure, as illustrated in Figure 3. The procedure was adequate to define wire gauge for flux and armature coil, tooth-tip geometry, winding fixture procedure and end-turn coil size. The field winding number of turns and wire gauge for both armature and field coils are presented on Table 2.

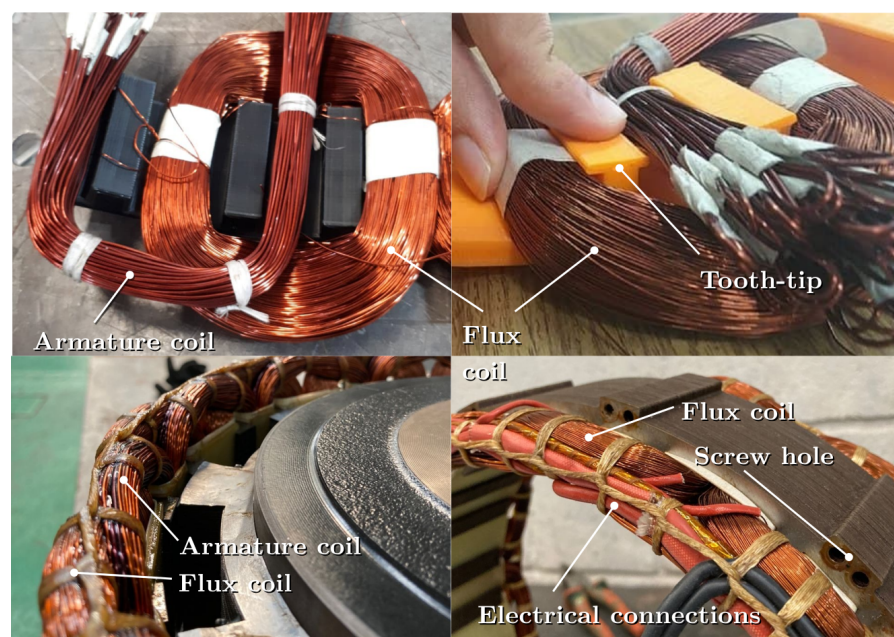


Figure 3. Manufacturing evaluation using a 3D-printed model, and final result in the built machine.

Although a lower air gap, such as tenths of millimeters, demands lower field current and higher power output, there is a higher chance of direct contact between rotor and stator. In-wheel machines demand mechanical structural evaluation in order to avoid possible catastrophic failure, which is especially troublesome considering the uncertainties of the manufacturing process. Electromagnetic design was evaluated considering different values for air gap, which lead to 0.5 mm as the less troublesome value. The final values are presented in Table 2, which presents some similarities to other published works [41,52].

Table 2. Dimensional limitations for the FSM.

Parameter	Symbol	Value	Unit
Outer radius	r_{out}	155	mm
Inner radius	r_{in}	111	mm
Axial length	l_a	51	mm
Air gap length	l_g	0.5	mm
Armature coil number of turns	N_a	15	-
Field coil number of turns	N_f	840	-
Armature wire gauge	ϕ_a	$2 \times 18 + 3 \times 21$	AWG
Field wire gauge	ϕ_f	27	AWG

3.2. Analytical Modeling

The analysis of the electrical machine performance must consider the double salient structure effect. In the proposed design methodology, a semi-analytical method provides accurate results with lower computational effort as compared to numerical methods. Thus, the magnetic field distribution is calculated using the Maxwell–Fourier method to evaluate the electric machine performance parameters. For early design stages, it offers great flexibility for assessing the electrical machine performance with several geometric parameters variation.

The electromagnetic performance of a machine is usually evaluated in literature considering motoring conditions. Additionally, the reluctance machine is commonly driven by a power converter with current control. In this case, the power converter is regarded as the current source and the magnetic field is calculated with defined current densities. In this case, the FSM behavior is similar to that of a salient pole synchronous machine [53,54].

The present work is based on cost reduction and simplicity. Thus, a passive diode rectifier is adopted to adequately generated three-phase alternating voltages to the vehicle 12 Vdc bus. The voltage level is controlled by manually adjusting the field current using a boost DC–DC converter. Since there is no inverter circuit, the machine performance is reduced due to the lack of a field position control.

The methodology discussed here is proposed for an early design stage, in which it is desirable to evaluate different topologies and geometric parameters. Therefore, the output power is calculated using a simplified model of a generator supplying a three-phase linear load. The challenge faced for analyzing the FSM in such a manner is related to its time-varying inductances that occur due to the double salient structure.

A first approximation is carried out with the field circuit's dynamic being neglected. The voltage equation in machine variables is defined as

$$v_{abc} = -R_s i_{abc} - \frac{d\lambda_{abc}}{dt} + e_{abc}. \quad (1)$$

A per-phase equivalent circuit model for steady state analysis is developed to evaluate the mechanical to electrical power conversion. The Equation (1) is solved for known harmonic components that showed a prominent effect over the generated power.

The generated voltage is evaluated for the FSM using an approximately sinusoidal waveform with a fundamental electrical frequency of ω_1 . This allows the armature-field mutual inductance to be simplified considering only its fundamental component, $M_{af,1}$. With a constant field current, i_f , no-load back-EMF is calculated by

$$E_{a,nl} = \omega_1 M_{af,1} I_f \quad (2)$$

The time-varying armature inductances are decomposed into their harmonic components. The amplitude and phase of these components are calculated in relation to the phase a circuit. In a balanced three-phase condition, these relations facilitate the definition of the harmonic effective inductances using a reasoning similar to that of a synchronous machine. The zero order component has a similar effect of the synchronous inductance, and is calculated from the phase a average value, $L_{aa,0}$, that is

$$L_{s,0} = \frac{3}{2} L_{aa,0}. \quad (3)$$

The other inductance harmonic components that affect average output power are the second and fourth order harmonics, which can be simplified into a per-phase effective inductance, calculated by

$$L_{s,2} = \frac{3}{2} L_{aa,2}, \quad (4)$$

$$L_{s,4} = \frac{3}{2} L_{aa,4}. \quad (5)$$

The load is simplified to a linear RL branch. With these approximations, the voltage Equation (1) can be expressed in complex notation as

$$\begin{aligned} E_{a,nl} - j\omega L_{s,0} I_{a,1} e^{-j\theta_{i,1}} \\ + j\omega L_{s,2} e^{j2\theta_{i,1}} I_{a,1} e^{-j\theta_{i,1}} + j\omega L_{s,4} I_{a,5} e^{-j\theta_{i,5}} \\ = (R_{load} + j\omega L_{load}) I_{a,1} e^{-j\theta_{i,1}}, \end{aligned} \quad (6)$$

where $I_{a,1}$ and $\theta_{i,1}$ are the amplitude and phase of the fundamental component of phase current, $I_{a,1}$ and $\theta_{i,1}$, respectively. It can be noticed that despite of the approximated sinusoidal generated voltage, the inductance harmonic component yields a frequency coupling with the fifth order current, $I_{a,5} \angle -\theta_{i,5}$. With the considered harmonic components, the voltage equation for this current harmonic is expressed as

$$\begin{aligned} j5\omega L_{s,4} I_{a,1} e^{-j\theta_{i,1}} - j5\omega L_{s,0} I_{a,5} e^{-j\theta_{i,5}} \\ = (R_{load} + j5\omega L_{load}) I_{a,5} e^{-j\theta_{i,5}}. \end{aligned} \quad (7)$$

Concerning the evaluation of steady-state power conversion, only the fundamental component is considered. From Equation (6), it can be observed that the harmonic inductance components affect the fundamental circuit behavior. This can be interpreted as a demagnetization effect, which is dependent on the loading conditions. To further clarify this behavior, these demagnetizing terms can be characterized as equivalent RL branches. First, the second order inductance term is evaluated by its admittance frequency response. This transfer function is used to calculate a parallel RL branches with similar behavior, that is

$$\begin{aligned} -\frac{1}{j\omega L_{s,2} e^{j2\theta_{i,1}}} &= Y_{eq}(j\omega) \\ &= \frac{1}{R_1 + j\omega L_1} + \frac{1}{R_2 + j\omega L_2}. \end{aligned} \quad (8)$$

The fourth order inductance term is evaluated using Equation (7). This term is related to the fifth harmonic order of the phase current, but the effect is over the fundamental circuit. The resultant per-phase fundamental circuit is presented in Figure 4.

The second order inductance term equivalent RL branch is calculated by

$$R_{eq,2,r1} = \frac{(R_{load} + R_{eq,4})L_{s,2}}{2(L_{s,0} + L_{load} + L_{eq,4} - L_{s,2})}, \quad (9)$$

$$L_{eq,2,r1} = \frac{L_{s,2}}{2}, \quad (10)$$

$$L_{eq,2,r2} = -L_{s,2}. \quad (11)$$

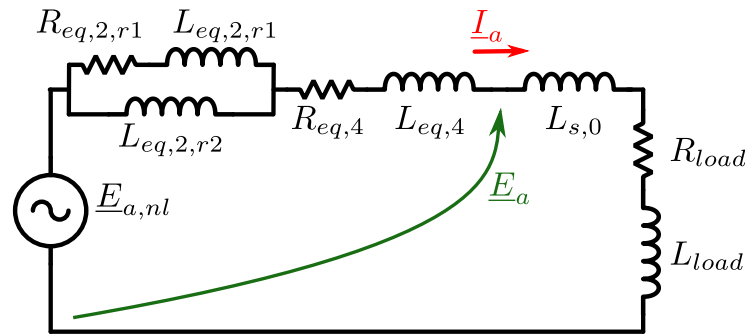


Figure 4. Per-phase FSM equivalent circuit.

The fourth order inductance harmonic effect is evaluated the equivalent RL calculated by

$$R_{eq,4} = \frac{5\omega^2 L_{s,4}^2 R_{load}}{(R_{load}^2 + 25\omega^2 (L_{s,0} + L_{load})^2)}, \quad (12)$$

$$L_{eq,4} = -\frac{25\omega^2 L_{s,4}^2 (L_{s,0} + L_{load})}{(R_{load}^2 + 25\omega^2 (L_{s,0} + L_{load})^2)}. \quad (13)$$

This equivalent circuit is used to optimize the generated power. As discussed, the time-varying inductance components have a demagnetizing effect, which reduces the no-load internal generated voltage, $E_{a,nl}$. Considering the resultant magnitude and angle variation, the internal induced voltage, E_a , is calculated. The power converted from mechanical to electrical form is given by

$$P_{conv} = \frac{3}{2} \Re(E_a \cdot I_a^*). \quad (14)$$

The assessment of the proposed steady-state equivalent circuit is validated with a dynamic simulation result for the converted power. The machine voltage equation is solved considering the time-varying inductances using numerical integration method. These inductances are calculated using the Maxwell–Fourier method, but any method can be used to analyze the magnetic field distribution. The field circuit dynamics is discarded and the field current is defined constant. The result is presented in Figure 5. The converted power calculated with the equivalent circuit shows excellent agreement with the average power calculated over an electrical cycle in the dynamic simulation, with an error of less than 0.01%.

Due to the high number of turns for the field winding, each coil has an equivalent resistance of 36.3 Ω . Since the machine was designed targeting micro-hybrid application and, thus, voltage levels below 48 V, the field coils were connected in parallel. Using a series connection would demand voltages up to 200 V. According to the constructive characteristics of the machine, each field coil has a different reluctance path, and each one

is mutually coupled and varies unequally over time. That increases the complexity in order to represent the circuit with an equivalent inductance.

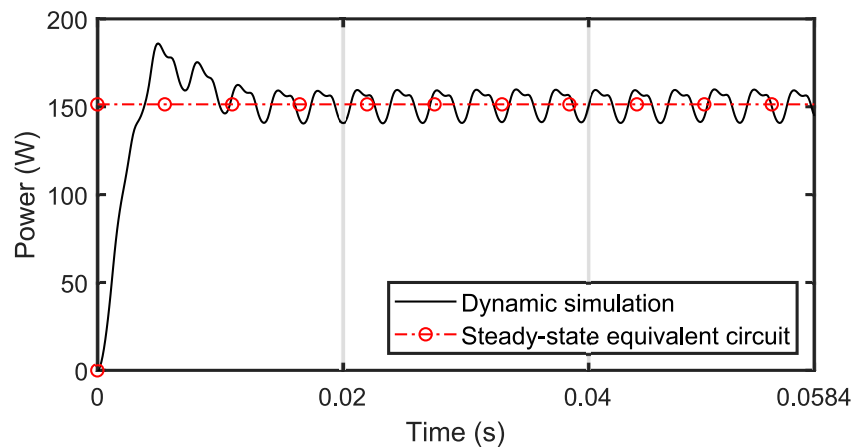


Figure 5. Converted power comparison between proposed steady-state equivalent circuit and dynamic simulation.

Thus, the model to represent this machine requires an individual evaluation of each field coil, leading to an equivalent electrical circuit with 15 variables, 12 for the field circuit and 3 for the armature phases.

The armature winding DC resistance is approximated considering an ideal conductor to evaluate resistive losses. The total armature and field resistance is estimated with Equation (15). It is defined using the winding total number of turn per coil, N_{coil} , the winding fill factor, k_{Cu} , the slot area, A_{slot} , and the electrical resistivity of copper, ρ_{Cu} . The winding fill factor is equal to 0.4, which is in accordance with the adopted value in the literature [55,56].

$$R_{coil} = l_{turn} \frac{\rho_{Cu}}{k_{Cu} (A_{slot}/2)} N_{coil}^2 \quad (15)$$

The average length of a coil turn, l_{turn} , is calculated with stack length, l_s , and an estimate of the end-turn length, l_{end} , that is

$$l_{turn} = 2l_s + 2l_{end} \quad (16)$$

In this work, the end-turn length is approximated with the average coil circumferential span, l_{circ} , and the axial length extending outward from the machine active length, l_{axis} , being expressed as

$$l_{end} = l_{circ} + 2l_{axis} \quad (17)$$

where

$$l_{circ} = \frac{1}{2} [2\alpha_s + (2\alpha_s - \beta_{sa})] r_{wind} \quad (18)$$

and

$$l_{axis} = \frac{\beta_{sa}}{2} r_{wind} \quad (19)$$

The method adopted for evaluating the winding inductances, the Maxwell–Fourier method, is based on the premise of an iron core with infinity magnetic permeability. The magnetic field distribution is not evaluated in the core, where important phenomena occur. On the other hand, as proposed in [57], stator core teeth and yoke magnetic fluxes can be estimated using an equivalent magnetic circuit.

The tooth flux is obtained by calculating the average air gap flux density over the distance of a tooth pitch, from the mid-point of an adjacent slot opening to the other. With

the magnetic fluxes calculated for each tooth, φ_t , the linear equation system can be derived for the yoke fluxes, φ_y . In a 12 slot stator, the equation system is given as

$$\begin{bmatrix} -1 & 1 & 0 & \cdots & 0 \\ 0 & -1 & 1 & & 0 \\ \vdots & & & \ddots & \vdots \\ 0 & 0 & 0 & -1 & 1 \\ 1 & 1 & 1 & 1 & 1 \end{bmatrix} \begin{bmatrix} \varphi_{y1} \\ \varphi_{y2} \\ \vdots \\ \varphi_{y11} \\ \varphi_{y12} \end{bmatrix} = \begin{bmatrix} \varphi_{t1} \\ \varphi_{t2} \\ \vdots \\ \varphi_{t11} \\ 0 \end{bmatrix}. \quad (20)$$

3.3. Topology Considerations

There are some aspects that must be addressed before using optimization routines in the proposed application. Even at early design stages, constructive and material parameters must be accounted for when adopting simplified analytical methodology, such as used in the present work.

The flux-switching machine provides great design flexibility, with different rotor and stator structures. The use of different stator slot and rotor pole number combinations, winding configurations, and rotor structures offers distinct electromagnetic performances. In HEV drive applications, a FSM with 24 stator slots and 10 rotor poles (24s-10p) is proven to be a good candidate [47], and is considered as a base design for the presented work.

It has been discussed that machines presenting fewer stator slots and rotor poles can achieve a higher electromagnetic performance due to the smaller leakage magnetic flux [56]. However, keeping a constant magnetizing flux for a configuration with lower number of poles yields an increased stator and rotor yoke thickness to avoid saturation. Considering the geometric constraints in the present work, the increased stator and rotor yokes shortens the slots' depth, leading to a smaller slot area for placing the conductors. Moreover, adopting a topology with increased number of stator slots and rotor poles allows the use of a deeper slot, but a higher operation frequency increases core and converter switching losses.

Using the base structure of 24s-10p, three different FSM topologies are evaluated for the proposed application. Figure 6 presents the flux density for the configuration: 12s-5p, 24s-10p, and 36s-15p. With a fixed slot opening in relation with the slot pitch angle and a field excitation of 3.0 A/mm², the slot depth is adjusted in order to limit the yoke flux density below 1.3 T. These geometries parameters are used to calculate the inductances, and with the equivalent circuit, the converted power are calculated. The results are presented in Table 3.

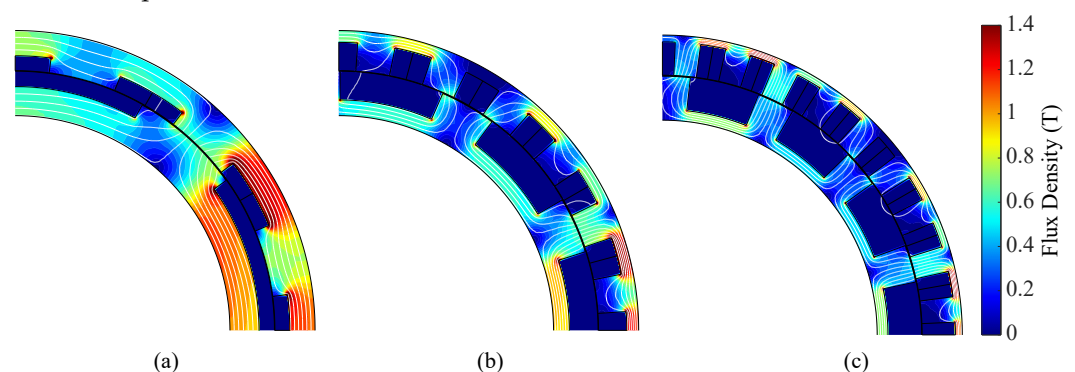


Figure 6. Flux density for three different topologies: (a) 12s-5p, (b) 24s-10p, and (c) 36s-15p.

Table 3. Output power comparison between the studied configurations.

Machine Topology	Output Power	Copper Losses
12s-5p	81 W	62 W
24s-10p	165 W	76 W
36s-15p	148 W	70 W

When evaluating different FSM configurations, some other guide rules are important to address. Using a rotor with an even pole number avoids unbalanced magnetic force, which creates a high mechanical stress, generating noise and vibration. The 10-pole machine has a lower torque ripple when compared to 8-pole and 4-pole configurations [58]. Lastly, the copper losses, as presented in Table 3, are slightly higher than other configurations, but with better output power results.

3.4. Structural and Material Limitations

The realization of initial electromagnetic performance evaluation must consider material properties, mechanical structure stress, and thermal limitations. Despite the chosen methodology for magnetic field analysis, the given geometric flexibility must avoid weak mechanical structures, thermal stresses, and magnetic saturation in order to realize a feasible design. In this context, the present section discusses the constructive constraints and material parameter limitations considered for the design procedure.

It is necessary to determine the slots fill factor, k_{cu} , to define the armature and field winding conductors. In machines that have circular conductors with random winding, the typical fill factor is between 0.3 and 0.5. A fill factor of 0.4 is commonly found in literature in FSM design [55,56] and is used in this work. With Equations (15)–(19), the armature and field winding copper losses are calculated. It is important to have a good estimate for the winding resistivity. The FSM operates at low speeds in direct drive in-wheel applications, in which copper losses are critical and represents a major part of the total machine losses [59,60].

The electric loading capability is determined by the winding insulation material and the ability of the cooling system to dissipate the produced heat. The FSM has the advantage of placing all field sources in the stator, resulting in a better thermal management. With the use of water jacket cooling systems, the use of values of surface current density up to 30 A/mm² are observed in the literature [41,47,59]. According to [55], machines with surface current densities higher than 10 A/mm² must consider a special cooling system. In the present work, the value of 10 A/mm² is adopted as the current density maximum limit.

It is possible to minimize the copper losses using conductors with higher cross section area, which requires slots with greater area. However, to reduce the volume of the magnetic core in order to increase the slot area can lead to core saturation, deteriorating the magnetic performance. For various standard machines (e.g., induction and synchronous machines), there are some permitted flux densities that can be applied in early design stages. Saturation effect is evaluated through magnetic field simulation using the finite element method. At no load condition, the saturation effect over induced voltage of the 24s-10p FSM topology is evaluated for different core magnetic paths, i.e., the teeth and yoke of the stator and rotor core. The ferromagnetic material adopted is the high performance NO30-16HP for electric vehicles application from Aperam South America.

Table 4 shows the magnetization level for different parts of the machine under test, in which the reduction in the electromotive force fundamental was limited to 5% compared to the unsaturated result. This same magnetizing condition applied to an ideal electric steel simulation gives the reference values for this work.

Each row presents the magnetic flux density result at different core parts for each test, where the machine is simulated considering the magnetically non-linear material. Furthermore, the permitted flux densities are obtained from the last column results, which are derived for a machine with an ideal core. This is suitable for simplified methodologies for evaluation of electromagnetic performance at early design stages, such as those proposed in this work.

Considering the approximate teeth and yoke magnetic flux densities calculation, as discussed in the prior section, the stator teeth and yoke magnetization should be limited to 1.8 T and 1.5 T, respectively. According to the simulation results, the saturation on the stator teeth limits the machine design before the rotor teeth does. In addition, considering the flux distribution characteristics, adopting a rotor yoke with a thickness 5% shorter than

that of the stator yoke results in a similar flux density. Thus, only the stator flux density is analyzed.

Table 4. Evaluation of the saturation effect on the induced voltage.

Region Tested	Flux Density (T)				Linear Model Value
	Rotor Yoke	Rotor Teeth	Stator Yoke	Stator Teeth	
Rotor yoke	1.6	0.77	0.57	1.02	1.97
Stator yoke	0.45	0.65	1.62	0.88	1.95
Stator teeth	0.88	1.16	0.94	1.61	1.73

Defining the limits, considering both fill factor and core dimensioning to avoid magnetic saturation, allows the design procedure to take into account physical limitations of the machine. Therefore, the semi-analytic optimization of the FSM is carried with criteria, not being limited to the electromagnetic design. The proposed routine for motor design can be optimized using, for instance, formal multi-criteria optimization techniques. These provide solutions to problems with multiple and conflicting objectives.

4. Model Validation

The built prototype was not conceived for road validation, thus no ingress protection was considered. Evaluation tests were conducted on a testbench, and on a roller dynamometer using a real car. Before starting the operational tests the prototype was vacuum impregnated and isolation tests were performed within standard limits [61–63].

Presented results only consider the machine as a generator with electrical loads at the machine's terminals. Voltage and current were measured using oscilloscope probes, and later results were processed to calculate power. Mechanical torque was provided by an induction motor fed by a variable frequency drive responsible to adjust speed of the wheel. Figure 7 presents the test bench and the final setup using the real car.



Figure 7. Machine test bench (left) and vehicle evaluation (right).

In the worst case scenario, the machine rotates at low speed and flux must increase to produce torque. In that situation, losses are high and energy generation is low, leading to the lowest overall efficiency, as shown in Figure 8. A steady state field current of 7.2 A was drained resulting in a winding temperature of 80 °C.

The simulation results for induced considering parallel field winding connection are compared to the experimental results taken from a test bench. The FSM was driven by an induction motor fed by a variable frequency drive at 500 rpm and with the field circuit fed by an independent current source. Figure 9 shows the results of the no-load induced phase voltage when the total field current is 4.8 A. The parallel connection of the field coils tends to demagnetize the others fields, which leads to a lower induced voltage and output power.

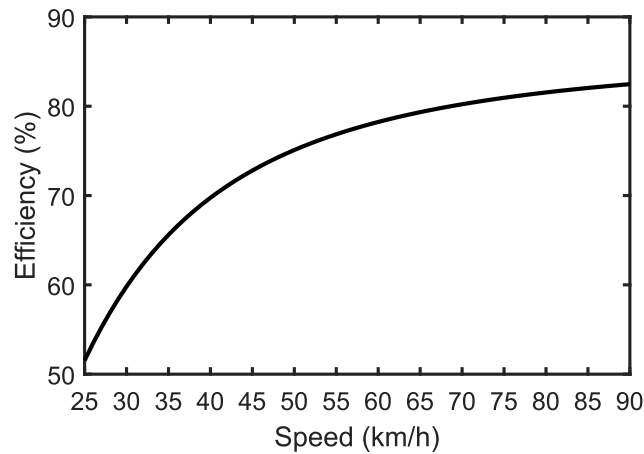


Figure 8. Proposed generator operating within urban driving cycles speed limits.

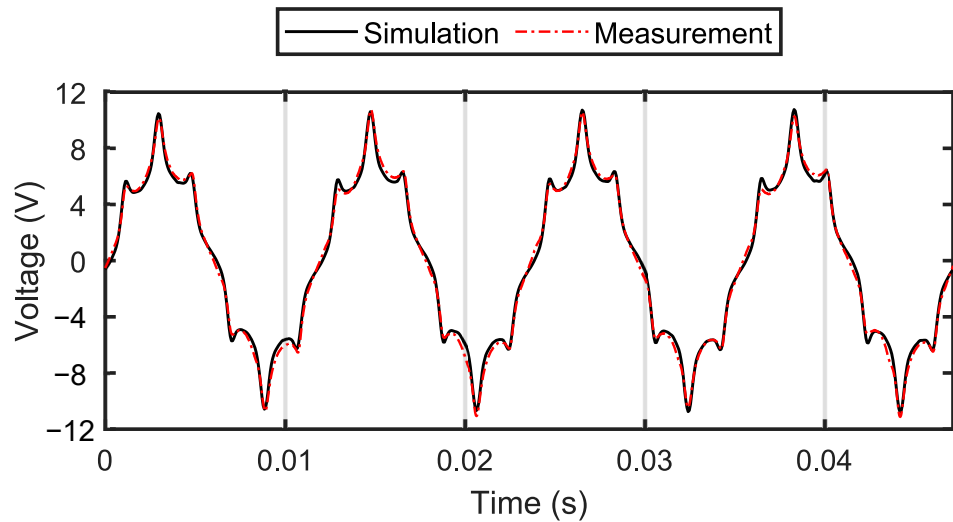


Figure 9. Induced phase voltage for a field current of $i_f = 4.8$ A parallel connected.

However, a series connection forces the current to be the same in each field coil, avoiding demagnetization, and producing an induced voltage nearly two times higher as compared to the parallel connection, as shown in Figure 10. The fundamental waveform is 82.5% higher, which increases the output power by 3.3 times.

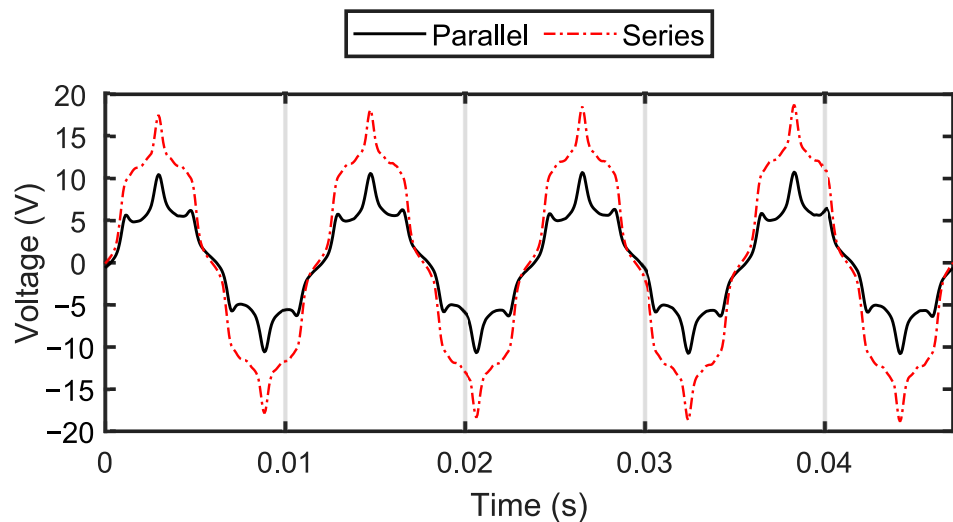


Figure 10. Induced phase voltage considering parallel and series connection of field coils.

Figure 11 shows the results of the induced line voltage for a total field current of 4.8 A with the armature terminals connected to a resistive load of 3.3Ω connected in delta.

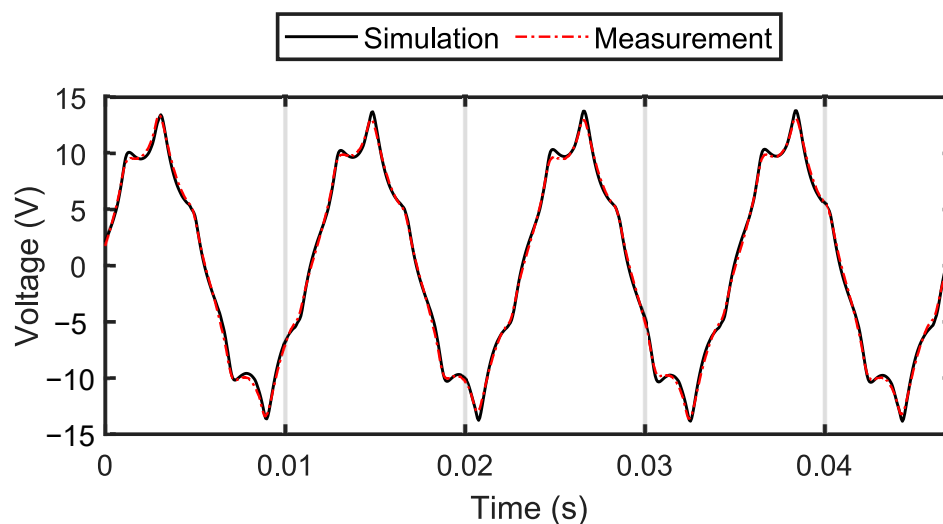


Figure 11. Induced line voltage feeding a 3.3Ω load.

In order to evaluate a series connected operation, a higher voltage is needed, which limits its capabilities to be boarded. Another alternative is to build a controlled current source for each coil which will be evaluated in future works.

5. Conclusions

In this paper, a flux-switching machine was designed and evaluated for a regenerative braking operation. The electromagnetic design was calculated using the Maxwell–Fourier analyses. By analysing the presented method, it is possible to obtain the field distribution calculation in a structure with double saliency with effectiveness. The calculated field distribution can also be used to evaluate the magnetizing level on the core.

The presented design was constrained by available space inside the wheel, which considered the minimum modifications to the vehicle, preserving the original vehicle drum brake. The machine output power is limited by the internal diameter and the low rotation speed. However, the development and construction process presented show the ground base limitations of the application, which can lead to a better performance for upcoming designs.

The performance was evaluated using the developed equivalent circuit and the machine model was validated using both the finite element method and experimental results. It has been established that keeping the current constant on the field coils prevents field demagnetizing and, consequently, power reduction.

Author Contributions: Conceptualization, G.A.M., L.C.M.S., B.J.C.F. and T.A.C.M.; methodology, G.A.M. and T.A.C.M.; software, G.A.M.; validation, G.A.M. and D.P.V.G.; formal analysis, G.A.M.; investigation, G.A.M. and D.P.V.G.; resources, L.C.M.S., T.A.C.M. and B.J.C.F.; data curation, D.P.V.G.; writing—original draft preparation, G.A.M., D.P.V.G. and T.A.C.M.; writing—review and editing, G.A.M., D.P.V.G. and T.A.C.M.; visualization, G.A.M., D.P.V.G., L.C.M.S., B.J.C.F. and T.A.C.M.; supervision, L.C.M.S., B.J.C.F. and T.A.C.M.; project administration, T.A.C.M. All authors have read and agreed to the published version of the manuscript.

Funding: This research received no external funding.

Institutional Review Board Statement: Not applicable.

Informed Consent Statement: Not applicable.

Data Availability Statement: The data that support the findings of this study are available from the corresponding author upon reasonable request.

Acknowledgments: This work has been supported by the Brazilian agency CAPES (Coordenação de Aperfeiçoamento de Pessoal de Nível Superior). Additionally, we would like to thank Aperam South America for the support in the realization of this work and the Graduate Program in Electrical Engineering—Universidade Federal de Minas Gerais.

Conflicts of Interest: The authors listed above have no conflict of interest to declare. All co-authors have agreed with the contents of the manuscript and there is no financial interest to report. We certify that the submission is an original work and is not under review at any other publication.

References

1. IEA. *Energy and Air Pollution*; Technical Report; International Energy Agency (IEA): Paris, France, 2016.
2. Mulholland, E.; Miller, J.; Braun, C.; Jin, L.; Rodríguez, F. Quantifying the long-term air quality and health benefits from Euro 7/VII standards in Europe. In *The International Council of Clean Transportation. ICCT Briefing June*; ICCT: San Francisco, CA, USA, 2021.
3. Coimbra, M.R.; Barbosa, T.P.; Vasques, C.M. A 3D-Printed Continuously Variable Transmission for an Electric Vehicle Prototype. *Machines* **2022**, *10*, 84. [[CrossRef](#)]
4. Nikowitz, M. *Advanced Hybrid and Electric Vehicles*; Springer International Publishing: Berlin/Heidelberg, Germany, 2016. [[CrossRef](#)]
5. Ismail, M.M.R.; Wira, J.Y.; Abu, A.; Abidin, M.A.Z. Thermal Energy Harvesting From Automotive Waste Heat. *Adv. Mater. Res.* **2012**, *516–517*, 498–503. [[CrossRef](#)]
6. Zhou, F.; Dede, E.; Joshi, S. Application of Rankine Cycle to Passenger Vehicle Waste Heat Recovery—A Review. *SAE Int. J. Mater. Manuf.* **2016**, *9*, 224–235. [[CrossRef](#)]
7. Maia, T.A.; Faria, O.A.; Barros, J.E.; Porto, M.P.; Cardoso Filho, B.J. Test and simulation of an electric generator driven by a micro-turbine. *Electr. Power Syst. Res.* **2017**, *147*, 224–232. [[CrossRef](#)]
8. Simões, A.N.; Carvalho, D.J.; Morita, E.d.S.; Moretti, H.L.; Vendrameto, H.V.; Fu, L.; Torres, F.; Souza, A.N.d.; Bizzo, W.A.; Mazon, T. A Triboelectric Nanogenerator for Energy Harvesting from Transformers' Vibrations. *Machines* **2022**, *10*, 215. [[CrossRef](#)]
9. Carneiro, P.M.; Ferreira, J.A.; Kholkin, A.L.; Soares dos Santos, M.P. Towards Self-Adaptability of Instrumented Electromagnetic Energy Harvesters. *Machines* **2022**, *10*, 414. [[CrossRef](#)]
10. Aksu, U.; Halicioglu, R. A review study on energy harvesting systems for vehicles. *Teh. Glas.* **2018**, *12*, 251–259. [[CrossRef](#)]
11. Abdelkareem, M.A.A.; Xu, L.; Ali, M.K.A.; Elagouz, A.; Mi, J.; Guo, S.; Liu, Y.; Zuo, L. Vibration energy harvesting in automotive suspension system: A detailed review. *Appl. Energy* **2018**, *229*, 672–699. [[CrossRef](#)]
12. Da Silva, J.F.F.G. Challenges for the Electric Mobility Transition: Lessons from Norway and Perspectives for Brazil. Master's Thesis, FGV, Rio de Janeiro, Brazil, 2019.
13. Cardoso, D.S.; Fael, P.O.; Espírito-Santo, A. A review of micro and mild hybrid systems. *Energy Rep.* **2020**, *6*, 385–390. [[CrossRef](#)]
14. Chau, K.T.C. *Electric Vehicle Machines and Drives: Design, Analysis and Application*; John Wiley & Sons: Hoboken, NJ, USA, 2015.
15. Picron, V.; Fournigault, D.; Baudesson, P.; Armiroli, P. Cost-Efficient Hybrid Powertrain System with 48 V Network. *ATZ Worldw.* **2012**, *114*, 46–50. [[CrossRef](#)]
16. Li, C.; Guo, X.; Fu, J.; Fu, W.; Liu, Y.; Chen, H.; Wang, R.; Li, Z. Design and Analysis of a Novel Double-Stator Double-Rotor Motor Drive System for In-Wheel Direct Drive of Electric Vehicles. *Machines* **2021**, *10*, 27. [[CrossRef](#)]
17. Sollicec, G.L.; Chasse, A.; Van-Frank, J.; Walser, D. Dual Mode Vehicle with In-Wheel Motor: Regenerative Braking Optimization. *Oil Gas Sci. Technol. Rev. D'IFP Energies Nouv.* **2013**, *68*, 95–108. [[CrossRef](#)]
18. Lambert, T.; Biglarbegian, M.; Mahmud, S. A novel approach to the design of axial-flux switched-reluctance motors. *Machines* **2015**, *3*, 27–54. [[CrossRef](#)]
19. Sabri, M.F.M.; Danapalasingam, K.A.; Rahmat, M.F. A review on hybrid electric vehicles architecture and energy management strategies. *Renew. Sustain. Energy Rev.* **2016**, *53*, 1433–1442. [[CrossRef](#)]
20. Spichartz, P.; Bokker, T.; Sourkounis, C. Comparison of electric vehicles with single drive and four wheel drive system concerning regenerative braking. In Proceedings of the 2017 Twelfth International Conference on Ecological Vehicles and Renewable Energies (EVER), Monte Carlo, Monaco, 11–13 April 2017. [[CrossRef](#)]
21. European Commission. Commission Regulation (EU) 2017/1151 of 1 June 2017 supplementing Regulation (EC) No. 715/2007 of the European Parliament and of the Council on type-approval of motor vehicles with respect to emissions from light passenger and commercial vehicles (Euro 5 and Euro 6) and on access to vehicle repair and maintenance information, amending Directive 2007/46/EC of the European Parliament and of the Council, Commission Regulation (EC) No. 692/2008 and Commission Regulation (EU) No. 1230/2012 and repealing Commission Regulation (EC) No. 692/2008. *Off. J. Eur. Union* **2017**, *175*, 1–643.
22. Cui, M.; Zhao, S.; Deguchi, Y.; Chen, C.; Fan, D. Performance of flux switching integrated starter-generator system with dual-mode control circuit. *Int. J. Mechatron. Autom.* **2018**, *6*, 94. [[CrossRef](#)]
23. Viorel, I.A.; Szabó, L.; Löwenstein, L. Integrated starter-generators for automotive applications. *Acta Electroteh.* **2004**, *45*, 7.
24. Mirahki, H.; Moallem, M.; Rahimi, S.A. Design Optimization of IPMSM for 42 V Integrated Starter Alternator Using Lumped Parameter Model and Genetic Algorithms. *IEEE Trans. Magn.* **2014**, *50*, 114–119. [[CrossRef](#)]

25. Bu, F.; Liu, H.; Huang, W.; Hu, Y.; Degano, M.; Gerada, C.; Rajashekara, K. Induction-Machine-Based Starter/Generator Systems: Techniques, Developments, and Advances. *IEEE Ind. Electron. Mag.* **2020**, *14*, 4–19. [[CrossRef](#)]
26. Wang, W.; Chen, X.; Wang, J. Motor/Generator Applications in Electrified Vehicle Chassis—A Survey. *IEEE Trans. Transp. Electrif.* **2019**, *5*, 584–601. [[CrossRef](#)]
27. Xu, W.; Zhao, H.; Ren, B.; Chen, H. A regenerative braking control strategy for electric vehicle with four in-wheel motors. In Proceedings of the 2016 35th Chinese Control Conference (CCC), Chengdu, China, 27–29 July 2016. [[CrossRef](#)]
28. Rizzo, G.; Naghinajad, S.; Tiano, F.; Marino, M. A Survey on Through-the-Road Hybrid Electric Vehicles. *Electronics* **2020**, *9*, 879. [[CrossRef](#)]
29. Zhao, X.; Kou, B.; Huang, C.; Zhang, L. Optimization design and performance analysis of a reverse-salient permanent magnet synchronous motor. *Machines* **2022**, *10*, 204. [[CrossRef](#)]
30. Ocana, I.M.; Baker, N.J.; Mecrow, B.C.; Gan, C.; Hilton, C.; Brockway, S. Testing of an in-wheel Halbach array motor. In Proceedings of the 2020 International Conference on Electrical Machines (ICEM), Gothenburg, Sweden, 23–26 August 2020. [[CrossRef](#)]
31. Wang, X.; Wu, L.; Zhou, S.; Hu, C.; Zhao, M. Optimization Design of In-wheel Motor Based on Halbach (Ce,Nd)FeB Magnet. In Proceedings of the 2019 22nd International Conference on Electrical Machines and Systems (ICEMS), Harbin, China, 11–14 August 2019. [[CrossRef](#)]
32. Gao, P.; Gu, Y.; Wang, X. The Design of a Permanent Magnet In-Wheel Motor with Dual-Stator and Dual-Field-Excitation Used in Electric Vehicles. *Energies* **2018**, *11*, 424. [[CrossRef](#)]
33. Akatsu, K.; Fukuda, K. Advanced Control Method of 5-Phase Dual Concentrated Winding PMSM for Inverter Integrated In-Wheel Motor. *World Electr. Veh. J.* **2021**, *12*, 61. [[CrossRef](#)]
34. Agamloh, E.; von Jouanne, A.; Yokochi, A. An Overview of Electric Machine Trends in Modern Electric Vehicles. *Machines* **2020**, *8*, 20. [[CrossRef](#)]
35. Jahns, T. Getting Rare-Earth Magnets Out of EV Traction Machines: A review of the many approaches being pursued to minimize or eliminate rare-earth magnets from future EV drivetrains. *IEEE Electr. Mag.* **2017**, *5*, 6–18. [[CrossRef](#)]
36. Boldea, I.; Tutelea, L.N.; Parsa, L.; Dorrell, D. Automotive Electric Propulsion Systems With Reduced or No Permanent Magnets: An Overview. *IEEE Trans. Ind. Electron.* **2014**, *61*, 5696–5711. [[CrossRef](#)]
37. Fujishiro, S.; Ishikawa, K.; Kikuchi, S.; Nakamura, K.; Ichinokura, O. Design of outer-rotor-type multipolar switched reluctance motor for electric vehicle. *J. Appl. Phys.* **2006**, *99*, 08R324. [[CrossRef](#)]
38. Nikam, S.P.; Rallabandi, V.; Fernandes, B.G. A High-Torque-Density Permanent-Magnet Free Motor for in-Wheel Electric Vehicle Application. *IEEE Trans. Ind. Appl.* **2012**, *48*, 2287–2295. [[CrossRef](#)]
39. Goto, H. Double Stator Axial-Flux Switched Reluctance Motor for Electric City Commuters. In Proceedings of the 2018 International Power Electronics Conference (IPEC—Niigata 2018—ECCE Asia), Niigata, Japan, 20–24 May 2018. [[CrossRef](#)]
40. Patel, N.R.; Shah, V.A.; Lokhande, M.M. A Novel Approach to the Design and Development of 12/15 Radial Field C-Core Switched Reluctance Motor for Implementation in Electric Vehicle Application. *IEEE Trans. Veh. Technol.* **2018**, *67*, 8031–8040. [[CrossRef](#)]
41. Ahmad, N.; Khan, F.; Ali, H.; Ishaq, S.; Sulaiman, E. Outer rotor wound field flux switching machine for In-wheel direct drive application. *IET Electr. Power Appl.* **2019**, *13*, 757–765. [[CrossRef](#)]
42. Ali, H.; Sulaiman, E.; Kosaka, T. Design and performance analysis of various high torque segmented rotor HE-FSM topologies for aircraft applications. *IET Electr. Power Appl.* **2020**, *14*, 297–304. [[CrossRef](#)]
43. Tang, Y.; Motoasca, E.; Paulides, J.J.; Lomonova, E.A. Comparison of flux-switching machines and permanent magnet synchronous machines in an in-wheel traction application. *COMPEL Int. J. Comput. Math. Electr. Electron. Eng.* **2012**, *32*, 153–165. [[CrossRef](#)]
44. Raminosoa, T.; El-Refaie, A.M.; Pan, D.; Huh, K.K.; Alexander, J.P.; Grace, K.; Grubic, S.; Galioto, S.; Reddy, P.B.; Shen, X. Reduced Rare-Earth Flux-Switching Machines for Traction Applications. *IEEE Trans. Ind. Appl.* **2015**, *51*, 2959–2971. [[CrossRef](#)]
45. Cao, Y.; Zhu, S.; Yu, J.; Liu, C. Optimization Design and Performance Evaluation of a Hybrid Excitation Claw Pole Machine. *Processes* **2022**, *10*, 541. [[CrossRef](#)]
46. Dmitrievskii, V.; Prakht, V.; Kazakbaev, V.; Anuchin, A. Comparison of Interior Permanent Magnet and Synchronous Homopolar Motors for a Mining Dump Truck Traction Drive Operated in Wide Constant Power Speed Range. *Mathematics* **2022**, *10*, 1581. [[CrossRef](#)]
47. Sulaiman, E.B.; Khan, F.; Kosaka, T. Field-Excited Flux Switching Motor Design, Optimization and Analyses for Future Hybrid Electric Vehicles Using Finite Element Analyses. *Prog. Electromagn. Res. B* **2016**, *71*, 153–166. [[CrossRef](#)]
48. Mendonça, G.; Maia, T.; Filho, B.C. Magnetic Field Analytical Solution for Non-homogeneous Permeability in Retaining Sleeve of a High-Speed Permanent-Magnet Machine. *Math. Comput. Appl.* **2018**, *23*, 72. [[CrossRef](#)]
49. Mendonça, G.A.; Maia, T.A.C.; de Jesus Cardoso Filho, B. Improved Semi-Analytical Magnetic Field Solution For High-Speed Permanent-Magnet Machines With Permeable Retaining Sleeve Including Diffusion Effect. *Prog. Electromagn. Res. B* **2020**, *88*, 97–118. [[CrossRef](#)]
50. Ramakrishnan, K.; Curti, M.; Zarko, D.; Mastinu, G.; Paulides, J.J.H.; Lomonova, E.A. Comparative analysis of various methods for modelling surface permanent magnet machines. *IET Electr. Power Appl.* **2017**, *11*, 540–547. [[CrossRef](#)]
51. Ehsani, M.; Gao, Y.; Longo, S.; Ebrahimi, K.M. *Modern Electric, Hybrid Electric, and Fuel Cell Vehicles*; CRC Press: Boca Raton, FL, USA, 2018.

52. Nguyen, H.Q.; Jiang, J.Y.; Yang, S.M. Design of a 12-slot 7-pole wound-field flux switching motor for traction applications. In Proceedings of the 2016 IEEE International Conference on Industrial Technology (ICIT), Taipei, Taiwan, 14–17 March 2016. [[CrossRef](#)]
53. Yang, S.M.; Zhang, J.H.; Jiang, J.Y. Modeling torque characteristics and maximum torque control of a three-phase, dc-excited flux-switching machine. *IEEE Trans. Magn.* **2016**, *52*, 1–4. [[CrossRef](#)]
54. Balyovski, T.; Ilhan, E.; Tang, Y.; Paulides, J.; Wijnands, C.; Lomonova, E. Control of DC-excited flux switching machines for traction applications. In Proceedings of the 2014 Ninth International Conference on Ecological Vehicles and Renewable Energies (EVER), Monte-Carlo, Monaco, 25–27 March 2014; pp. 1–5.
55. Amara, Y.; Hoang, E.; Gabsi, M.; Lécrivain, M.; Allano, S. Design and comparison of different flux-switch synchronous machines for an aircraft oil breather application. *Eur. Trans. Electr. Power* **2005**, *15*, 497–511. [[CrossRef](#)]
56. Zhou, Y.J.; Zhu, Z.Q. Comparison of Wound-Field Switched-Flux Machines. *IEEE Trans. Ind. Appl.* **2014**, *50*, 3314–3324. [[CrossRef](#)]
57. Abbaszadeh, K.; Alam, F.R. On-Load Field Component Separation in Surface-Mounted Permanent-Magnet Motors Using an Improved Conformal Mapping Method. *IEEE Trans. Magn.* **2016**, *52*, 1–12. [[CrossRef](#)]
58. Sulaiman, E.B.; Kosaka, T.; Matsui, N. Design study and experimental analysis of wound field flux switching motor for HEV applications. In Proceedings of the 2012 XXth International Conference on Electrical Machines, Marseille, France, 2–5 September 2012; pp. 1269–1275.
59. Omar, M.F.; Sulaiman, E.; Jenal, M.; Kumar, R.; Firdaus, R.N. Magnetic Flux Analysis of a New Field-Excitation Flux Switching Motor Using Segmental Rotor. *IEEE Trans. Magn.* **2017**, *53*, 1–4. [[CrossRef](#)]
60. Khan, F.; Sulaiman, E.; Ahmad, Z. A novel wound field flux switching machine with salient pole rotor and nonoverlapping windings. *Turk. J. Electr. Eng. Comput. Sci.* **2017**, *25*, 950–964. [[CrossRef](#)]
61. *Std 1799-2012*; Recommended Practice for Quality Control Testing of External Discharges on Stator Coils, Bars, and Windings. IEEE: Piscataway, NJ, USA, 2012; pp. 1–48. [[CrossRef](#)]
62. *Std 1434-2000*; Guide to the Measurement of Partial Discharges in Rotating Machinery. IEEE: Piscataway, NJ, USA, 2000; pp. 1–64. [[CrossRef](#)]
63. *Std 43-2013 (Revision of IEEE Std 43-2000)*; Recommended Practice for Testing Insulation Resistance of Electric Machinery. IEEE: Piscataway, NJ, USA, 2014; pp. 1–37. [[CrossRef](#)]